Nanofilament formation and regeneration during Cu/Al_2O_3 resistive memory switching

William A. Hubbard,[†,‡] Alexander Kerelsky,[†,‡] Grant Jasmin,[†,‡] E. R. White,[†,‡] Jared Lodico,[†,‡] Matthew Mecklenburg,[¶] and B. C. Regan[*,†,‡]

Department of Physics and Astronomy, University of California, Los Angeles, CA 90095, U.S.A., California NanoSystems Institute, University of California, Los Angeles, CA 90095, U.S.A., and Center for Electron Microscopy and Microanalysis, University of Southern California, Los Angeles, California, 90089, U.S.A.

E-mail: regan@physics.ucla.edu

Abstract

Conductive bridge random access memory (CBRAM) is a leading candidate to supersede flash memory, but poor understanding of its switching process impedes widespread implementation. The underlying physics and basic, unresolved issues such as the connecting filament's growth direction can be revealed with direct imaging, but the nanoscale target region is completely encased and thus difficult to access with real-time, high-resolution probes. In $Pt/Al_2O_3/Cu$ CBRAM devices with a realistic topology, we find that the filament grows backwards towards the source metal electrode. This observation, consistent over many cycles in different devices, corroborates the standard electrochemical metallization model of CBRAM operation. Time-resolved scanning transmission electron microscopy (STEM) reveals distinct, nucleation- and potential-limited no-growth periods occurring before and after a connection is made respectively. The sub-femtoampere ionic currents visualized move some thousands of atoms during a switch, and lag the nanoampere electronic currents.

[*]To whom correspondence should be addressed

[†]Department of Physics and Astronomy, UCLA

[‡]California NanoSystems Institute, UCLA

[¶]Center for Electron Microscopy and Microanalysis, USC

Keywords

ReRAM, RRAM, CBRAM, *in situ* TEM

Introduction

A next-generation non-volatile memory technology will ideally achieve more speed and endurance while requiring less space and power than the present standard.[1] In FLASH memory a logical "1" or "0" is signaled by a channel conductance that is controlled by moving electrons onto or off of a nearby floating gate. In resistive random access memory (ReRAM) the analogous conductance is controlled by moving atoms in the channel itself. Because atoms are more ponderous and less self-repulsing than electrons, ReRAM's direct approach has the potential to outperform FLASH for many non-volatile memory applications.[2,3] However, the atomic mass transport fundamental to ReRAM operation involves physics and chemistry that is more complicated and unfamiliar than that seen in traditional microelectronic devices, where

the constituent atoms do not rearrange themselves into new geometric configurations as part of normal device function.

Conductive bridge memory (CBRAM), also known as electrochemical metallization bridge (EMB) or programmable metallization cell (PMC) memory, is among the most promising types of ReRAM,[2–4] and represents an archetype of this new paradigm of mechanically reconfigurable microelectronic circuitry. In their pristine, as-fabricated state, CBRAM devices consist of an "active" electrode separated from an "inactive" electrode by an insulating layer. According to the standard picture,[5,6] applying a positive voltage bias to the active electrode ionizes active metal atoms (e.g. Cu or Ag) and drives them through the insulator to be reduced at the inactive metal electrode. With continuing mass transport these displaced atoms form a conducting filament that grows backwards towards the active metal electrode, eventually bridging the two electrodes (ON state). Applying negative bias reverses the growth and eventually breaks the filament (OFF state).

Refining this simple, qualitative picture of CBRAM into a detailed model[5,7] is not straightforward, and many uncertainties remain. The chemical reactions, field-assisted diffusion, Joule-heating, and mechanical stresses that dictate these switching processes have crucial, and in some cases unknown interrelationships over length scales varying from atomic to micrometer, and times scales spanning picoseconds to years.[3,4] Matters as basic as the connecting filament's growth direction are still controversial.[8–13]

To gain insight into the governing physics, the mechanical evolution of CBRAM devices is observed with transmission electron microscopy (TEM), which has unparalleled ability to achieve real-time, atomic resolution in bulk material. Three main approaches have been adopted, each of which strikes a different balance between the incompatible goals of good TEM imaging access and realistic CBRAM device architecture. The first approach deploys electrolyte-coated wires or wedges[14,15] in a nanomanipulation stage to form devices *in situ*. These devices are irregular, with stress and field gradients that affect the switching dynamics.[16] The second approach, cutting cross sections from vertical stacks,[17–21] begins with a more realistic initial geometry. However, the necessary sample preparation with a focused ion beam (FIB),[17,18] ion mill,[19,21] or chemical-mechanical polishing[20] introduces damage, contamination, and exposed interfaces that are not present in a deployed ReRAM device.[22] The third approach microfabricates horizontal devices specifically for TEM measurements[15] to avoid such post-processing, but these devices have an unrealistic, exposed interface connecting the electrodes which is vulnerable to surface migration[23,24] and environmental effects.[25]

These three architectures have produced various results. Only a few share video documenting real-time observations.[14,15,21] None of the studies on microfabricated CBRAM devices have shown multiple ON–OFF cycles. Among the CBRAM results,[14,15,17–21] most[14,15,17,18,21] report conducting bridges that grow from the active towards the inert electrode, a result that contradicts the standard model[5,6] and has led to debate[8–13] about the root mechanisms.

The slant-vertical architecture we employ allows for high-quality, real time TEM imaging without compromising the native ReRAM topology. The resultant devices can be cycled repeatedly, demonstrating this essential characteristic of rewritable memory. The device fabrication follows the usual deposition order of bottom electrode, electrolyte, and top electrode, but introduces a horizontal offset between the bottom and top electrodes (Fig. 1a). This "slant" version of the standard, vertical ReRAM stack allows a clear line-of-sight through the switching region. It also gives clean, regular, microfabricated device geometries that can be reproduced on a wafer scale, while avoiding problematic post-processing and spurious interfaces. The amorphous, conformal ALD coating, deposited after the Pt but before the Cu electrode, precludes an interface connecting the inactive and active electrodes (Fig. S1); any conducting path between the electrodes must penetrate the insulating layer, as in a vertically-stacked device. Finally, the hor-

izontal offset can be lithographically adjusted from positive to negative (overlapping) values, which enables exploration of the continuum between good imaging access and a true vertical stack.

Figure 1b shows an annular dark-field (ADF) STEM image of a slant-vertical device before any biasing. Ramping the potential bias on the Cu electrode relative to the (grounded) Pt electrode gave little current until the device impedance abruptly dropped by several orders of magnitude at 4.4 V (see Fig. S2). At this point the electronic transport became limited by the programmed current compliance of 50 nA and the applied voltage dropped to 1–2 V, for a device impedance of 20–40 MΩ. This condition represents the successful creation of a tunneling junction between the electrodes,[7] and is defined to be the ON or low resistance state (LRS). Smaller device impedances can be arranged by increasing the compliance current.[5] This device switched a half dozen times *in situ*, and the data give no indication that such cycling could not have continued (Fig. S2).

Concurrent with the abrupt impedance change in the device of Fig. 1b, a structure appeared in the gap between the electrodes. To reveal this subtle structure we aligned and subtracted images acquired "before" and "after", and rescaled the resultant image's intensity to better fill the available dynamic range. The resultant "difference image" Fig. 1c shows the appearance of a single filament connecting the electrodes, and the disappearance of material from the Cu electrode. On the side nearer the Cu electrode, the filament terminates in the semi-circular region with the most dramatic material loss (Fig. 1c inset).

Video and transport data from a similar device (Figs. 2 and 3, supplementary video S1) reveal the time-resolved dynamics of filament formation and cycling. In the pristine device of Fig 2a, as with the device of Fig. 1b-c, steadily ramping the voltage bias from zero gave small current increases initially. (All of the data reported in this Letter were obtained under quasi-static, as opposed to pulsed, switching conditions.) Once above 4.6 V the current jumped to the compliance limit of 50 nA. At this con-

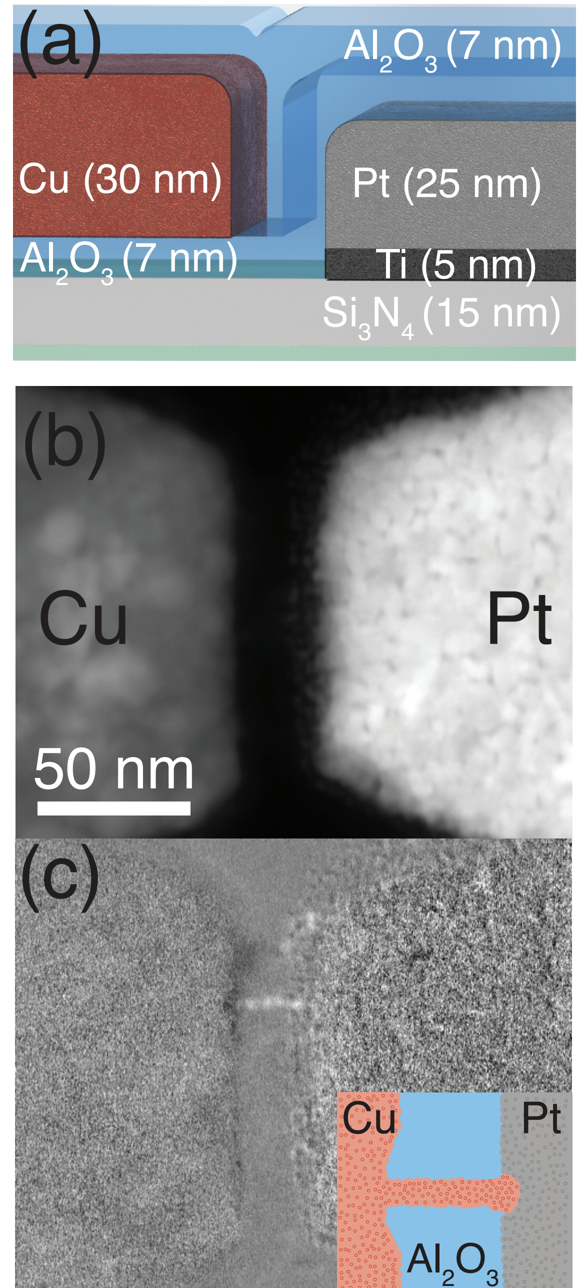

Figure 1: **Device schematic, STEM image, and difference image showing a filament.** (a) Slant-vertical device schematic, side view. The first ALD layer separates the electrodes and the second protects the Cu electrode from oxidation and surface migration. (b) STEM image of a completed device prior to biasing, plan view. (c) The result of subtracting (b) from an image of the device after a filament (pictured in the schematic inset) formed (Fig. S2). Bright/dark regions correspond to gain/loss of signal.

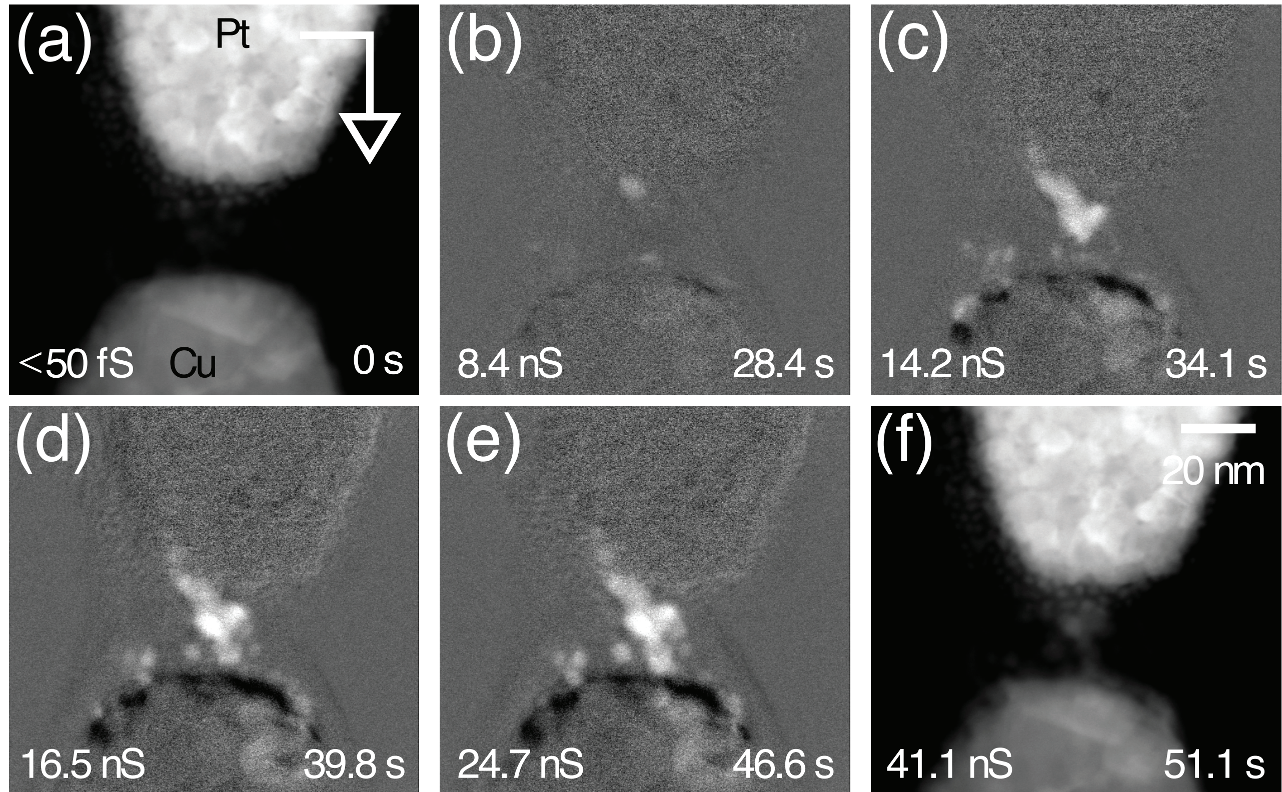

Figure 2: **Time-resolved filament growth.** STEM images of a device before (a) and after (f) filament formation, generated by averaging over several frames of video S1 to reduce noise. The filament spanning the gap is clearly visible in (f) without differencing. Subtracting (a) from frames 24, 29, 34, and 41 of video S1 gives the difference images shown in (b–e), respectively. As material disappears from the active electrode, a filament grows backwards from the inert electrode to bridge the gap. The frames used to generate (a–f) are indicated in gray in Fig. 3.

stant current level the voltage dropped steadily from 4 to 1 V over the next 22 s. The device resistance stabilized below 25 MΩ (Fig. S3), with an OFF/ON resistance ratio of more than 10^3.

The difference images 2b through 2e, constructed with identical contrast scales using 2a as the reference image, provide snapshots of the device's morphological evolution during this voltage drop. While material was disappearing from the Cu electrode, a filament grew from the Pt electrode until it reached the Cu electrode. We find the appearance of the filament simultaneous with disappearance of material from the Cu electrode to be compelling evidence that the filament is, in fact, copper. Thus copper was leaving the anode, migrating unseen across the gap, and depositing on the cathode to form a filament that eventually grew back to the anode. Taken together with the electrical data, these images corroborate the main features of the standard electrochemical metallization model.[5,6]

To provide a static summary of the entire video, including the switches occurring after the forming just described, in Fig. 3b we plot the average STEM intensity in three regions of interest (ROI): the eventual location of the complete filament, the edge of the Cu electrode, and the area where the filament terminates over the Cu electrode (Fig. S4). Also shown is a digital determination of the gap in the filament (Fig. S5). During forming the intensity in the copper ROI decreased while the intensity in the filament ROI increased, reflecting the net relocation of copper from the active electrode to the filament. The subsequent (switching) mass transport was relatively minor. However, in the third, much smaller filament-termination ROI

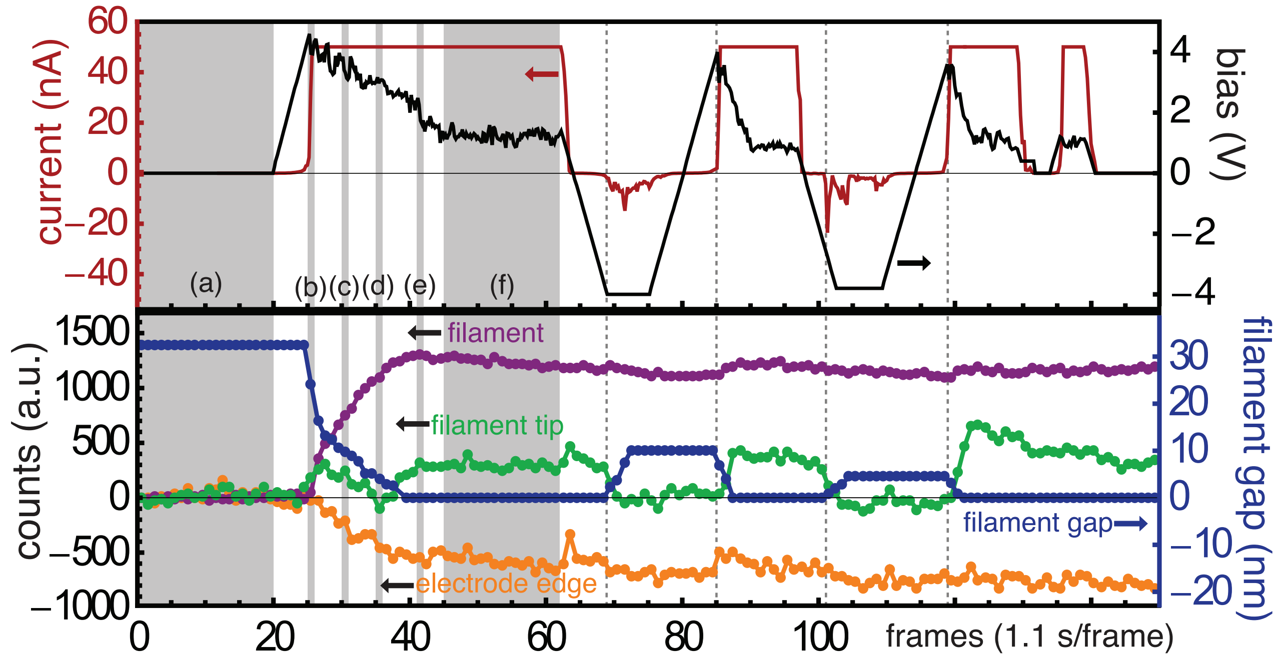

Figure 3: **CBRAM sequence FORM/RESET/SET/RESET/SET/READ applied to the device of Fig 2.** (top) Current and voltage vs. time. (bottom) Digital analysis of the simultaneously-acquired video S1. Shown are the average intensity in ROIs (Fig. S4) encompassing the entire final filament (purple), the edge of the copper electrode (orange), and the filament termination (green). The gap (blue) between the filament tip and the Cu electrode is also shown (Fig. S5). Gray bands indicate the frames that generate Fig. 2a–f. The initiation of a gap change is marked by the "b" band or a grey dashed line. Current compliance precedes every filament completion, and the gap self-limits at −4 V.

the video intensity manifested a clear square-wave synchronous with the electrical switching signals seen directly above; additional material appeared during the ON half-cycle, and disappeared during the OFF half-cycle. The gap also cycled synchronously with the electrical transport data, decreasing to zero during forming, and opening and closing 5–10 nm as the device switched (Fig. S3). Thus the video signal shows that the toggling of the resistance state between ON and OFF is accomplished by moving just a few thousand atoms. This estimate, based on crystalline copper's number density of 85 nm^{-3}, represents an upper limit; the copper density in the filament and thus the number of atoms moved is likely smaller.

Figures 2 and 3 (or the more complete video S1) give a rich, time-resolved view of the switching dynamics. Three distinct transport regimes are observed in every OFF to ON half cycle. The initial phase has no detectable growth, very little current, and is evidently nucleation limited. The first frame showing growth is coincident with the jump to current compliance. Surprisingly, the electrical current is fully developed before the switch closes, implying the transient existence of an undetected conduction path. With positive feedback from field concentration and Joule heating, this "leader" path likely determines the subsequent filament geometry. In an analogy with lightning propagation,[26] electrons traveling in one direction set up the more visible return stroke going the other way. (Compare Fig. 6 of ref. 4 and Fig. 1.3 of ref. 26.)

After the nucleation event the growth phase occurs, with the voltage decreasing and the electric field increasing as the gap closes under constant current. The total applied power decreases as the gap closes, but the power density in the gap is constant to the extent that the cross sectional of area of the current path

does not change. Thus this constant-current filament growth mode naturally incorporates feedback that regulates the maximum temperature and maintains a steady growth rate. In every case the filament enters a final, zero-growth phase, which can only be voltage limited (at ∼1 V) since the electric field across the near-zero tunneling gap is maximal.

The RESET shrinkage rates are comparable to the SET growth rates. In contrast to SET, the final stages of the RESET are electric field-limited (or, equivalently, the required overpotential is a function of the filament geometry), since the filament ceases to shrink while the voltage is held constant at -4V. The RESET process also evidently electropolishes the filament tip, ridding it of growth sites, since a nucleation overpotential is again required to reinitiate growth during the subsequent SET. While much of the filament remains, the increases in the device conductance resulting from FORM and SET are reversed by a RESET: the resultant OFF state shows resistance comparable to that of a pristine, unswitched device. Without the RESET, applying a 1 V READ voltage after the third cycle in Fig. 3 takes the device immediately into compliance, confirming that the contact is non-volatile.

With repeated cycling the filaments in these devices grow consistently toward the active electrode during SET, and reproducibly form tunneling electrical contacts. Cycling another device similar to those of Figs. 1–3 gave the video and transport data summarized in Fig. 4. Over the course of 10 cycles, a few thousand Cu atoms moved back and forth in a 3 nm junction region at the end of the filament nearest the active electrode (video S2, Fig. S7). (This particular device was switched over 40 times under various imaging and biasing conditions. Although it was still switching normally, the experiment was ended at this point because contamination deposited by the electron beam on the sample had begun to obscure the active region.) The material's rearrangement was slightly asymmetrical, occurring in a more concentrated region on the filament than the electrode (Figs. 4e, S3, S6). The geometric asymmetry between the electrode and filament, which is invoked to explain the switching bipolarity,[7,27] thus also appeared in this redistribution. As with the devices in Figs. 1–3, the evident hysteresis in the IV relationship here, with currents at ∼1 V higher after a SET than before the SET, is characteristic of ReRAM (or memristor[28]) behavior.

For this study, using small compliance currents gave filament growth times of many seconds, allowing for detailed imaging of the growth process. The time-resolved, approximately constant growth rates showed no sign of thermal runaway.[4] With ∼200 nW switching power and ALD alumina's thermal conductivity $\kappa = 2$ W/K·m,[29] the implied temperature rise inside a device is $\Delta T \simeq 100\,\mathrm{K}(\mathrm{nm}/d)$ where d is a length scale of order 1–10 nm. Thus switching with such low currents kept these devices near ambient temperature and reduced confounding thermal effects.

Working with larger compliance currents we saw very different dynamics. The devices showed sudden changes, a wider variety of filament geometries, evidence of annealing , and ON states with resistances $< 1\,\mathrm{k}\Omega$. With these switching parameters the devices could not be cycled more than once. We infer that increasing the compliance current in our devices increases the switching temperature above a critical threshold, leading to thermal runaway and much poorer cycling characteristics. The different filament morphologies and switching characteristics (*e.g.* filament growth direction) seen in other imaging studies[12,14,17,18,21] might be due in part to the larger (microampere) currents used.

For ReRAM in general, smaller compliance currents give larger, highly-non-linear ON-state resistances, minimize irreversible effects that are detrimental to endurance, and more closely approach the minimal dissipation condition desired for dense, low-power memory.[30] As small as they are, however, these currents are still far larger than the electrochemical ideal. Filaments such as those imaged here are formed with a time-integrated oxidation/reduction current of order $10^4 e = 1.6$ fC. The charge transported during forming and switching is more than 10^6 times larger, demonstrating that, of the contri-

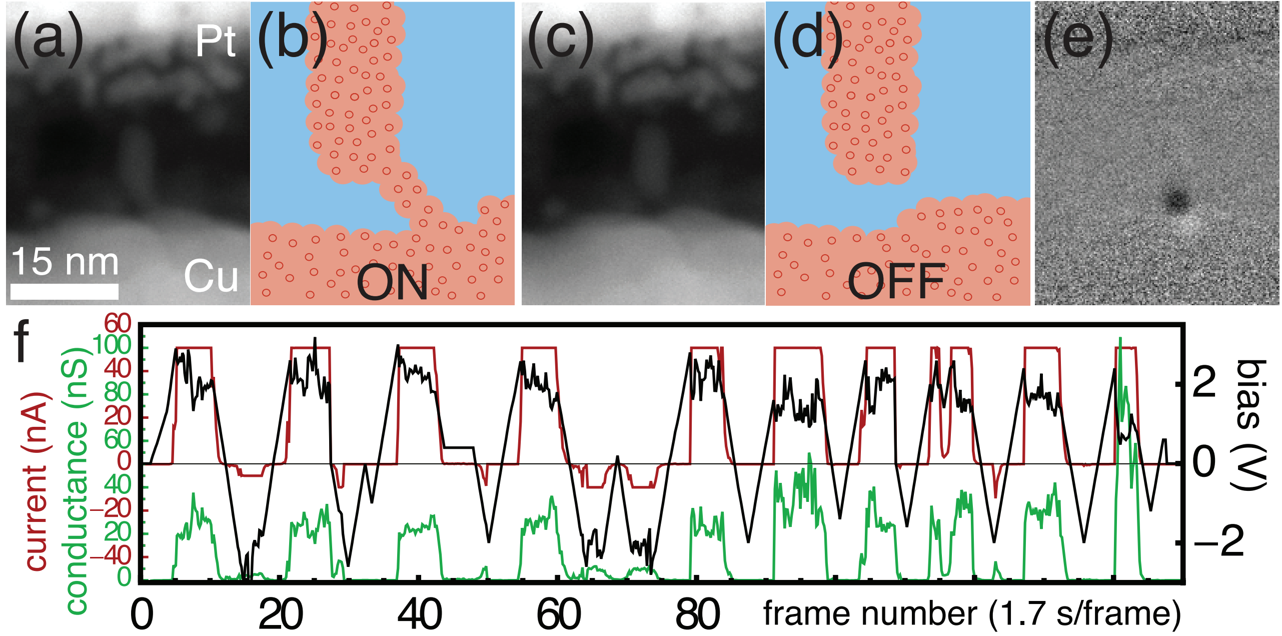

Figure 4: **Imaging and transport data for 10 switching cycles.** (a) STEM image of a device's ON states averaged over ten cycles, with schematic (b). (c) The corresponding average of OFF states, with schematic (d). (e) Difference image OFF-ON, i.e. (c−a). (f) Conductance, current, and device bias vs. time during the period spanned by (a, c, and e). See Figs. S6, Fig. S7, and video S2.

butions to the total cell current $I_{\text{cell}} = I_{\text{ion}} + I_{\text{el}}$, the ion current I_{ion} is negligible in comparison to the collateral electron current I_{el} (ref. 7) for this quasi-DC switching. With pulsed switching, larger compliance currents, and correspondingly higher temperatures the ion and electron currents would be more comparable ($1\ \mu\text{A}\cdot 10\ \text{ns} = 6 \times 10^4 e$).

In conclusion, we have observed CBRAM switching over many cycles with *in situ* STEM. The slant-vertical Cu/Al_2O_3 devices imaged are clean, microfabricated, and without spurious interfaces connecting the electrodes. During FORM and SET the conducting bridge filaments grow backwards towards the Cu active electrode, a result in agreement with the standard electrochemical metallization model.[5,6] We see the filament growth occurring after the jump in the total electronic current. This unexpected time-ordering indicates that the Al_2O_3 electrolyte supports a (leader) conduction path after Cu ions have penetrated the insulator, but before the filament is fully developed. Upon RESET both the visible filament connection and the leader conduction paths are evidently destroyed, as the device conductance reverts to a negligible value. Switching with compliance currents 10–100 times smaller than those used in standard CBRAM increases the filament formation and dissolution times by factors $\sim 10^9$, which highlights the crucial role of device self-heating. With the filaments' morphological evolution effectively in "slow-motion", fine details such as distinct nucleation and potential-limited periods within a CBRAM switching cycle are time-resolved.

Acknowledgement The authors thank Steve Kramer for helpful discussions. This work has been supported by FAME, one of six centers of STARnet, a Semiconductor Research Corporation program sponsored by MARCO and DARPA, and by National Science Foundation award DMR-1206849. The authors acknowledge the use of instruments at the Electron Imaging Center for NanoMachines supported by NIH 1S10RR23057 and the CNSI at UCLA.

Supporting Information Available:

Supporting information includes fabrication and imaging details, supplementary Figs. S1–7, and videos S1–2. This material is available free of charge via the Internet at `http://pubs.acs.org/`.

References

(1) Meijer, G. I. *Science* **2008**, *319*, 1625–1626.

(2) Emerging Research Devices, *International technology roadmap for semiconductors (ITRS)* **2013**,

(3) Fujisaki, Y. *Japanese Journal of Applied Physics* **2013**, *52*, 040001.

(4) Waser, R.; Dittmann, R.; Staikov, G.; Szot, K. *Advanced Materials* **2009**, *21*, 2632–2663.

(5) Yu, S.; Wong, H. S. P. *IEEE Transactions on Electron Devices* **2011**, *58*, 1352–1360.

(6) Valov, I.; Waser, R.; Jameson, J. R.; Kozicki, M. N. *Nanotechnology* **2011**, *22*, 254003.

(7) Menzel, S.; Tappertzhofen, S.; Waser, R.; Valov, I. *Physical Chemistry Chemical Physics* **2013**, *15*, 6945.

(8) Valov, I.; Waser, R. *The Journal of Physical Chemistry C* **2013**, *117*, 11878–11880.

(9) Gao, S.; Song, C.; Chen, C.; Zeng, F.; Pan, F. *The Journal of Physical Chemistry C* **2013**, *117*, 11881–11882.

(10) Valov, I.; Waser, R. *Advanced Materials* **2013**, *25*, 162–164.

(11) Liu, Q.; Jun, S.; Lv, H.; Long, S.; Li, L.; Yin, K.; Wan, N.; Li, Y.; Sun, L.; Liu, M. *Advanced Materials* **2013**, *25*, 165–167.

(12) Celano, U.; Goux, L.; Belmonte, A.; Opsomer, K.; Franquet, A.; Schulze, A.; Detavernier, C.; Richard, O.; Bender, H.; Jurczak, M.; Vandervorst, W. *Nano Letters* **2014**, *14*, 2401–2406.

(13) Clima, S.; Sankaran, K.; Chen, Y. Y.; Fantini, A.; Celano, U.; Belmonte, A.; Zhang, L.; Goux, L.; Govoreanu, B.; Degraeve, R.; Wouters, D. J.; Jurczak, M.; Vandervorst, W.; Gendt, S. D.; Pourtois, G. *physica status solidi (RRL) – Rapid Research Letters* **2014**, *8*, 501–511.

(14) Xu, Z.; Bando, Y.; Wang, W.; Bai, X.; Golberg, D. *ACS Nano* **2010**, *4*, 2515–2522.

(15) Yang, J. J.; Strukov, D. B.; Stewart, D. R. *Nature Nanotechnology* **2012**, *8*, 13–24.

(16) Park, G.-S.; Kim, Y. B.; Park, S. Y.; Li, X. S.; Heo, S.; Lee, M.-J.; Chang, M.; Kwon, J. H.; Kim, M.; Chung, U.-I.; Dittmann, R.; Waser, R.; Kim, K. *Nature Communications* **2013**, *4*.

(17) Liu, Q.; Sun, J.; Lv, H.; Long, S.; Yin, K.; Wan, N.; Li, Y.; Sun, L.; Liu, M. *Advanced Materials* **2012**, *24*, 1844–1849.

(18) Sun, J.; Liu, Q.; Xie, H.; Wu, X.; Xu, F.; Xu, T.; Long, S.; Lv, H.; Li, Y.; Sun, L.; Liu, M. *Applied Physics Letters* **2013**, *102*, 053502.

(19) Kudo, M.; Arita, M.; Ohno, Y.; Fujii, T.; Hamada, K.; Takahashi, Y. *Thin Solid Films* **2013**, *533*, 48–53.

(20) Choi, S.-J.; Park, G.-S.; Kim, K.-H.; Cho, S.; Yang, W.-Y.; Li, X.-S.; Moon, J.-H.; Lee, K.-J.; Kim, K. *Advanced Materials* **2011**, *23*, 3272–3277.

(21) Tian, X.; Wang, L.; Wei, J.; Yang, S.; Wang, W.; Xu, Z.; Bai, X. *Nano Research* **2014**, *7*, 1065–1072.

(22) Mayer, J.; Giannuzzi, L. A.; Kamino, T.; Michael, J. *MRS Bulletin* **2007**, *32*.

(23) Peppler, K.; Reitz, C.; Janek, J. *Applied Physics Letters* **2008**, *93*, 074104.

(24) Valov, I. *ChemElectroChem* **2014**, *1*, 26–36.

(25) Peng, C.-N.; Wang, C.-W.; Chan, T.-C.; Chang, W.-Y.; Wang, Y.-C.; Tsai, H.-W.; Wu, W.-W.; Chen, L.-J.; Chueh, Y.-L. *Nanoscale Research Letters* **2012**, *7*, 1–6.

(26) Dwyer, J. R.; Uman, M. A. *Physics Reports* **2014**, *534*, 147–241.

(27) Schindler, C.; Thermadam, S.; Waser, R.; Kozicki, M. *IEEE Transactions on Electron Devices* **2007**, *54*, 2762–2768.

(28) Strukov, D. B.; Snider, G. S.; Stewart, D. R.; Williams, R. S. *Nature* **2008**, *453*, 80–83.

(29) Cappella, A.; Battaglia, J.-L.; Schick, V.; Kusiak, A.; Lamperti, A.; Wiemer, C.; Hay, B. *Advanced Engineering Materials* **2013**, *15*, 1046–1050.

(30) Schindler, C.; Weides, M.; Kozicki, M. N.; Waser, R. *Applied Physics Letters* **2008**, *92*, 122910.

Graphical TOC Entry